PREDICTIONS OF SONAR PERFORMANCE FOR THE BASELINE TEST CASE: THE SIGNIFICANCE OF ECHO TIME SPREADING LOSSESS

Z. Y. Zhang, Defence Science and Technology Organisation, Edinburgh, SA 5111, Australia
R. Miyamoto, Applied Physics Laboratory, University of Washington, Seattle, WA 98105, USA

Sonar equation parameters were computed for the baseline test case of the David Weston Memorial Symposium on the Validation of Sonar Performance Assessment Tools, Cambridge, 7 – 9 April 2010. The effective time spread of the echo were estimated based on angular energy flux considerations. Time spreading due to the vacuum sphere target is negligible. The multipath channel spreads the echo energy significantly, leading to significant reduction in peak signal power.
Echo shape, ambient noise directivity, reverberation intensity, and signal processing effects were predicted using analytical expressions. The results highlight the significance of echo spreading in time domain for short CW and broadband coherent waveforms. Spreading losses in beam and Doppler domain due to angular and frequency spreading were also briefly discussed. The analytical approach complements predictions by numerical methods.

1 INTRODUCTION

1.1 Time Spreading and Transmission Loss

In active sonar, the signal is often spread out in time during multipath propagation to and from the target, and during the scattering process from the target. The echo energy is spread to a greater time extent, leading to a reduction in peak signal power in comparison with that would be obtained if the echo was a single amplitude-scaled, time-delayed, and Doppler-shifted replica of the transmitted pulse. This reduction may be called a time spreading loss. For broadband coherent pulses, the losses occur after correlation processing in the peak of the compressed echo and are also called correlation losses [Weston (1965)].

Therefore in active sonar, we may have the concept of an integrated transmission loss (ITL), where intensity from all significant multipaths are integrated with time, and peak transmission loss (PTL) where intensity from only overlapping multipaths are added. When the pulse length is long enough such that all significant multipaths overlap, PTL equals ITL. Similar principle applies to target strength and the definition of integrated and peak target strength.

Time spreading manifests as de-correlation in the frequency domain. For narrowband pulses, it leads to frequency fading. For broadband pulses, it limits the processing gain of conventional replica correlation regardless of the bandwidth of the transmitted pulse. Because of the mismatch between the echo and the replica, the signal energy cannot be compressed into a time-interval shorter than the inherent time spread due to target extent and channel multipath.

1.2 Angular Spreading and Spatial Correlation Length

Similar to time spreading loss, reduction in echo intensity occur when signal is spread to directions off-the main beam axis and side-lobes due to the angular spreading of the echo is greater than the beamwidth of the array. The loss places a limit on the beamforming gain that can be achieved regardless of the length of the array, because the signal energy cannot be compressed into a beam narrower than the signal angular spread.

Angular spreading leads to de-correlation in space. Signal de-correlation across array leads to correlation loss from beamforming compared to a single-direction plane wave. The loss depends on the correlation distance of the echo, which is inversely related to the angular spread of the signal. Zhang (2009) reviewed theoretical and experimental work on signal spatial de-correlation in shallow and deep waters and discussed its impact on beamforming gain.

The increase in SNR by the beamformer depends on the coherence of the signal versus the coherence of the noise across the array;

$$G_{bf} = G_s / G_n; \quad G_s = \sum_i \sum_j a_i a_j \rho_{s,ij}, \quad G_n = \sum_i \sum_j a_i a_j \rho_{n,ij} \tag{1}$$

Where G_s, G_n are signal and noise gain, a_i, a_j are amplitude shading coefficients of the i^{th} and j^{th} elements, $\rho_{s,ij}, \rho_{n,ij}$ are normalized spatial cross-correlation coefficients of the complex acoustic pressure received on the i^{th} and j^{th} elements for the signal and noise, respectively. The summations extend over all elements in the array.

When the acoustic pressure from the array is normalised by the number of array elements, M, the beamformer gain is unchanged, the normalized signal and noise gain are scaled as

$$g_{bf} = g_s / g_n = G_{bf}; \quad g_s = G_s / M^2, \quad g_n = G_n / M^2 \tag{2}$$

Considering an unshaded array, when it is steered to a plane wave signal, the signal is fully correlated across the array, the array has a normalized beam pattern with a normalized signal gain of unity. When the signal is partially correlated, the normalized signal gain is less than unity and represents a correlation loss in beam signal power due to signal de-correlation.

Amplitude shading affects both signal and noise gain and the array beam pattern. The receiver in the test cases is an un-shaded ($a_i, a_j = 1$) horizontal line array with uniform element spacing d and steered broadside. For the receiver and the noise conditions in the test cases, the normalized signal and noise gain in Eq.(2) reduces to

$$g_{s,n} = \frac{1}{M^2} \sum_{m=-(M-1)}^{M-1} (M - |m|) \rho_{s,n}(|m| d) \tag{3}$$

2 SONAR SCENARIO A2.I

The specifications of environment, waveforms, and sonar parameters for the baseline test case A2.I are in Zampolli & Ainslie (2010) and not repeated here.

Propagation and reverberation at longer ranges (over about 2 km in Case A2.I) are dominated by energy propagating at small grazing angles. A reasonable assumption that yields closed-form expressions for echo and reverberation is that bottom and surface losses are proportional to grazing angle, that is, the *intensity* reflection coefficient of the bottom and surface are approximated by

$$V_b(\theta) = \exp(-\alpha_b \theta), \quad V_s(\theta) = \exp(-\alpha_s \theta) \tag{4}$$

where θ is the grazing angle, and α_b, α_s are proportional constants. For the seafloor parameters in the test case, α_b can be easily found by Taylor expansion of the reflection coefficient near zero grazing angle, and equals about 0.5476, or 2.38 dB per radian.

For the ambient noise calculations, the source is an infinite 2D sheet of dipole sources. Both short and long propagation effects are important and we used the exact Rayleigh reflection coefficient.

Our formulation includes both bottom and surface losses for generality. For the baseline Test Case A2.I which has a smooth sea surface with no reflection loss, we have set $\alpha_s = 0$ in our calculations.

2.1 Noise Level and Directivity

The noise is specified to be generated by rain at a rain rate of 1 mm /hour. Rain noise is generated by direct forcing as rain strike the water surface and by wake cavity formation and bubble pulse oscillation as the rain drive down into the water. Bubble resonance oscillations generate a spectral

peak near 15 kHz, which is outside the frequency range of our consideration here. Rain noise below 10 kHz are mainly generated by raindrop impact impulses, which has a broadband spectrum with a negative slope. Due to the pressure-release surface, the noise on the surface radiates like dipoles whose strength can be estimated by Eqs.(60-63) of Ref.1 [APL-UW TR9407],

$$10\log A_0 = b + a\log RR - 10\log f; \quad 1 \le f \le 10; \quad RR \ge 10^{-2} \tag{5}$$

where A_0 is the source spectrum intensity at vertical incidence, the rain rate RR is in mm/hr, and frequency f is in kHz. The coefficients a & b are wind-speed dependent because wind causes raindrops falling at oblique incidence, roughens the sea surface and therefore affects rain noise generation. For wind speed less than 1.5 m/s, a = 25, b = 41.6.

Environmental conditions such as sound speed profile and sea floor reflectivity affect noise levels received. We note most rain noise data are collected in shallow water and assume that the above empirical equation for source intensity strength A_0 already included corrections due to effects of the environment of site where the data was collected. To account for multipath contribution in the shallow water test case environment, we used the formulation in Desharnais and Chapman (1999) to compute the total noise level N_0 received by an omni-directional receiver and the noise field directivities.

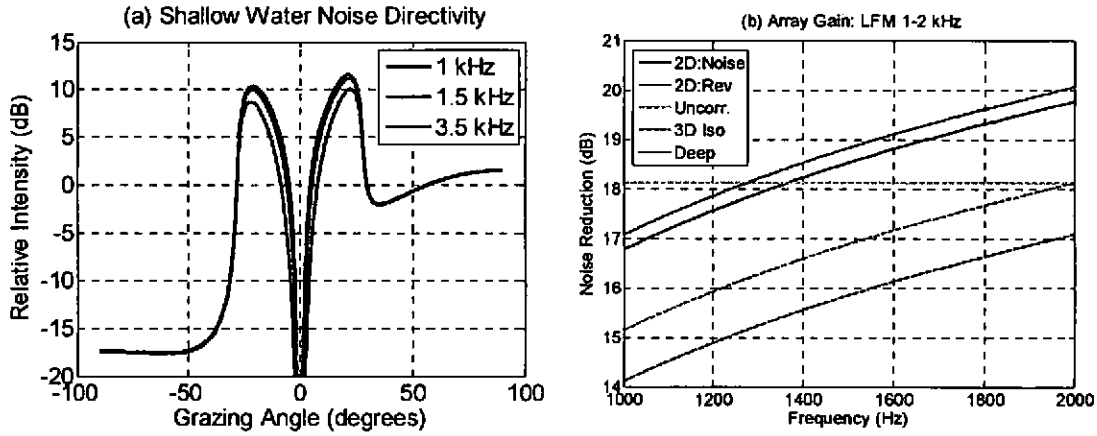

Figure 1(a) directivity of the rain noise in the shallow water waveguide. (b) noise reduction by the normalized beamformer for various types of noise directivity/correlations for the frequency range of the LFM pulse.

Figure 1(a) shows the directivity of the noise intensity relative to A_0, the intensity at vertical incidence in deep water. It is a composite effects of dipole radiation (which favors steep angles) and seafloor reflectivity (which favors shallow grazing angles). As a result, the peak of the directivity occurred at about 21 degrees instead of the critical angle of reflection of 28 degrees. Higher frequencies have lower levels because of greater in-water absorption.

2.2 Noise and Reverberation Reduction by Beamformer

Noise correlation can be obtained from its directivity [Cox, (1973)]. Here we take a simplified approach: the strong peaked directivity shown in Fig.1(a) prompts us to approximate the total noise field as the sum of two azimuthal isotropic noise fields [Burdic (1991)],

$$N(\theta) = N_+\delta(\theta - \theta_+) + N_-\delta(\theta - \theta_-) \tag{6}$$

where N_+ & N_- represent the noise intensity from above and below the receiver respectively, θ_+ & θ_- are the angles where the peaks occur in the upper and lower hemisphere (note that θ_- is defined as negative). The azimuthal isotropic noise fields are also referred to as 2-dimensional isotropic noise and their horizontal spatial correlation functions are respectively [Eq.(10-38), Burdic (1991)].

$$\rho_+(x) = J_0(kx\cos\theta_+), \quad \rho_-(x) = J_0(kx\cos\theta_-), \quad k = 2\pi f / c \tag{7}$$

Where x is the distance between two horizontal array elements.

The angles θ_+ & θ_- are almost symmetric at about 21 degrees and we make the approximation $\theta_0 \equiv \theta_+ = -\theta_-$. For horizontal arrays, noise from above and below the receiver contribute the same way to horizontal correlation and the total correlation function is

$$\rho_n(x) = \frac{N_+ J_0(kx\cos\theta_0) + N_- J_0[kx\cos(-\theta_0)]}{N_+ + N_-} = J_0(kx\cos\theta_0), \quad k = 2\pi f / c \qquad (8)$$

Figure 1(b) shows noise reduction by the normalized beamformer for various types of noise correlations in the frequency range of the LFM pulse. We use the term "noise reduction" to mean the Array Gain of a normalized beamformer whose signal gain has been normalized to unity. The black curve is for 2D azimuthal isotropic noise with grazing angle of 21 degrees, which we use for the rain noise in the waveguide. The red curve is for 2D azimuthal isotropic noise at zero grazing angle, which we use for reverberation from long range by the omni-directional source. The dashed green, magenta, and blue curves are for fully un-correlated, 3D isotropic, and deep water noise respectively. They are for comparison only and are not used in the subsequent calculations. Table 1 shows the various noise parameters for a rain rate of 1 mm/hr.

Table 1: Noise spectral level and reduction by the beamformer.

	CW 1 kHz	LFM 1.5 kHz	CW 3.5 kHz
Noise source spectrum intensity at vertical incidence, $10\log A_0$ (rain rate= 1 mm/hr), dB // μPa²/Hz/steradian @ 1 m	41.60	39.84	36.16
Noise spectral level in deep isovelocity water (no bottom reflections): $10\log(A_0\pi)$, dB// μPa²/Hz (For comparison only).	46.6	44.8	41.1
Noise spectral level in test case A2.I (multipath effects included), N_0, dB// μPa²/Hz	53.6	51.6	47.3
Rain noise reduction by beamformer: $10\log_{10}(1/g_n)$, dB	19.8	18.5	19.5
Reverberation reduction by beamformer: $10\log_{10}(1/g_R)$, dB (g_R is defined the same as g_n in section 1.2 with noise replaced by reverberation).	20.1	18.8	19.8

2.3 Pulse Parameters

For pulses, there are different definitions of time durations and band widths. Table 2 lists some parameters for the Gaussian pulses. The rectangular equivalent width refers to the width of a CW pulse of same peak intensity and energy. The rectangular equivalent width of the time-delay autocorrelation function is the same as the time resolution constant in Woodward (1964). There are also analogous definitions in frequency bandwidth. (Another definition, RMS widths, are related to estimation of the accuracy of range and Doppler measurements, and are different from the time resolution width defined here.)

For the rectangular LFM pulse, the rectangular equivalent width $T_{RE} = 2$ seconds. Because of its large time-bandwidth, its spectrum is nearly rectangular. The time domain autocorrelation function of its envelop approaches a sinc function with -3.9 dB points time width equals the reciprocal of its bandwidth. We approximate the sinc function by a rectangular equivalent pulse of 1 ms duration (= 1/bandwidth).

Table 2: Parameters of the Gaussian shaded CW Pulses

Waveform: $p(t) = A\cos(\omega_0 t)\exp[-(t\Delta\omega)^2/2]$, $\omega_0 = 2\pi f_0$, f_0 = 0.25, 1.0, 3.5 kHz, $\Delta\omega = \pi(\ln 2)^{-1/2} B_3$	
B_3: bandwidth: 3 dB power reduction points, Hz	$B_3 = f_0/20$ (as defined)
E_0: source pulse energy re μPa^2-s @ 1 m	$(A^2/2)\pi^{1/2}/\Delta\omega$
I_0: source pulse peak intensity re μPa^2 @ 1 m	$A^2/2$
T_3, time width: half-power (3 dB power reduction) points	$(4\ln 2)^{1/2}/\Delta\omega$
T_6, time width: half-amplitude (6 dB power reduction) points	$2^{1/2}T_3 = (8\ln 2)^{1/2}/\Delta\omega$
T_{RE}, time width: rectangular equivalent pulse of same peak & energy	$E_0/I_0 = \pi^{1/2}/\Delta\omega$
$R_f(\tau)$: time-delay auto-correlation function	$2E_0\exp[(\tau\Delta\omega)^2/4]\cos(\omega_0\tau)$
τ_R: time width of rectangular equivalent pulse of $R_f(\tau)$	$2^{1/2}T_{RE} = (2\pi)^{1/2}/\Delta\omega$

2.4 Echo Spatial Correlation

De-correlation of signal can occur in any direction in three dimensions. They can be characterized relative to the direction of signal propagation - radial, vertical, and transverse directions.

For the present scenario, we note that because the array is steered broadside and all its elements are also omni-directional, the array has no spatial extent in the radial and vertical direction. Therefore the angular spread of the multipath arrivals do not cause signal de-correlation loss. This is equivalent to saying that the spread in vertical angles of the multipath is much less than the omni-directional vertical beam width of the array, and all multipath energy are captured.

As reviewed and discussed in Zhang (2009), earlier work [e.g., Carey(1998), Wille and Thiele (1971)] on signal de-correlation in shallow water seems to indicate that at the higher end of frequencies, e.g., 3500 Hz, the transverse correlation length of the signal can be shorter than the array length of 32 wavelengths and there can be correlation losses of a few decibels. We also note that when the target is not in the Fraunhofer far field of the array [Ziomek (1995)], e.g., when the target is less than 6 km away from the array cut at 250 Hz, wave front curvature also introduces echo spatial de-correlation and consequently correlation losses. However, to limit the length of this paper, we will ignore signal spatial de-correlation losses in our later calculations and assume $g_s = 1$.

2.5 Scattering and Time Spreading from the Vacuum Sphere Target

Scattering from a vacuum sphere (pressure release boundary) is similar to scattering from a giant bubble without the bubble resonances (because there is no air inside). Compared to a rigid sphere, scattering from a vacuum sphere does not have interferences from creeping waves and the Rayleigh scattering region appear at much lower frequencies.

For the 5-m radius sphere, at frequencies greater than 1 kHz, the product of acoustic wavenumber-radius ka >> 1, and both vacuum and rigid sphere approach the target strength given by its geometric cross section $10\log(\pi a^2/4\pi)$ = 7.96 dB. The scattering is dominated by specular reflection from the front surface of the sphere, which has sharp δ -function like impulse responses with time spreading much shorter than the travel time from the front to the centre of the sphere [Sun et al (1991); Stanton&Chu (2008)]. This time spread is negligible compared to the time spread (122 ms) of the channel multipath.

We note that scattering from spheres tend to have broad main lobes near backscattering direction where the bistatic target strength remains constant over the effective grazing angles in shallow water waveguides. Propagation and scattering are then separable and the sonar equation is an accurate approximation [Ratilal et al (2002)].

2.6 Channel Effective Time Spread

We obtain an expression for the effective time spread of the channel by following Weston's (1971) energy flux approach, taking into account bottom and surface reflections and in-water absorption. The horizontal ray cycle distance in isovelocity water is $r_c = 2H/\tan\theta$. For each cycle, the ray undergoes one bottom and surface reflection, and absorption along the ray path $\alpha_v r_c/\cos\theta$. The number of cycles at range r is r/r_c. Hence the averaged decay of the energy flux with range is

$$\begin{aligned} f(r,\theta) &\propto (V_s V_b)^{(r/r_c)} \exp[-(\alpha_v r_c/\cos\theta)(r/r_c)] \\ &= \exp\{r[(\ln V_s + \ln V_b)\tan\theta/2H - \alpha_v/\cos\theta)]\} \end{aligned} \tag{9}$$

where $V_b(\theta), V_s(\theta)$ are the intensity reflection coefficients from the bottom and surface. Under the approximations $V_b(\theta) = \exp(-\alpha_b\theta)$, $V_s(\theta) = \exp(-\alpha_s\theta)$ and to 2nd order in small grazing angle, the energy flux is Gaussian distributed with grazing angle,

$$f(r,\theta) \propto \exp(-\alpha_v r)\exp(-\alpha\theta^2 r/2H) \tag{10}$$

where

$$\alpha = \alpha_s + \alpha_b + H\alpha_v \tag{11}$$

We take the effective angles as from zero to θ_e where the flux drops to exp(-1), i.e.,

$$\theta_e = (2H/\alpha r)^{1/2} \tag{12}$$

The effective angle decreases with range because boundary losses and absorption strip away energy at higher grazing angles. The ray's group velocity is $u = c\cos\theta$ and we take the effective time spread as the spread of travel times of all the rays between zero grazing angle and θ_e,

$$\tau_0 = (r/c)(1/\cos\theta_e - 1) \approx r\theta_e^2/2c = H/(c\alpha) \tag{13}$$

Where τ_0 is the effective time spread of the channel impulse response. Eq.(13) shows that the tendency for pulses to spread with range are counterbalanced by the shrinking of the effective angles with range, leading to a time spread essentially independent of range. Greater water depth increase multipath spacing and the time spread. More lossy boundaries strip away higher angle energy more quickly and decreases time spread. For test case A2.I, τ_0 is 121.7 ms at 250 Hz and 120.5 ms at 3500 Hz, the small difference being due to the increase of in-water absorption with frequency.

We note that when surface losses and in-water absorption are ignored, Eqs.(10-13) reduce to the corresponding equations in Harrison (2003), Prior & Harrison (2004), and Jones et al (2007), where the effects of bottom loss are considered.

2.7 Echo Intensity Envelope before Processing

We compute the averaged echo intensity as a function of time-delay by the convolution,

$$I_e(r,t) = I_0 u(t) \otimes h_2(r,t) \tag{14}$$

Where $I_0 = A^2/2$ is the source intensity at the peak of the transmitted pulses and $u(t)$ is the time-window,

$$u(t)=\begin{cases}\exp[-(t\,\Delta\omega)^2], & -T_H/2\le t\le T_H/2, \quad \text{Gaussian pulses}\\ 1, & -1\le t\le 1, \quad \text{LFM pulse}\end{cases} \tag{15}$$

and $h_2(r,t)$ is the flux impulse response of the 2-way propagation in terms of time delay $\tau=t-r/c$, adapted from [Harrison and Nielson (2007)] by adding in-water absorption and target cross section,

$$h_2(r,\tau)=\begin{cases}h_2^*(r,\tau), & 0\le\tau\le\tau_c,\\ h_2^*(r,\tau)(2/\pi)\sin^{-1}[2(\tau_c/\tau)-1], & \tau_c\le\tau\le 2\tau_c,\\ 0, & 2\tau_c\le\tau,\end{cases} \tag{16}$$

$$h_2^*(r,\tau)=\exp(-2\alpha_v r)(2\pi c)/(r^3H^2)\exp(-\tau/\tau_0)S_T, \quad 0\le\tau\le 2\tau_c \tag{17}$$

$$\tau_c=r\theta_c^2/(2c) \tag{18}$$

where we approximated the frequency-dependent in-water absorption by its value at the center frequency. The decay time $\tau_0=H/(c\alpha)$ is inversely proportional to α because lossy boundaries strip away higher angle energy more quickly. Equation (16) ignores all energy beyond the critical angle.

Figure 2 shows the flux-averaged echo intensity shape computed from Eq.(14) before processing. The Gaussian CW pulses are much shorter than the time spread of the exponential decay of the channel impulse response. Hence they act similar to δ(t) functions and the echoes look similar to the exponential impulse response with smoothened peaks. The drop in level with frequency is due to in-water absorption. The 2-sec LFM pulse reached its peak level after 0.4 second. The crosses in Figure 2(b) mark the time when the ray at critical angle arrives. The rapid dropoff after the critical angle shows the effects of truncation of the bottom reflectivity beyond the critical angle.

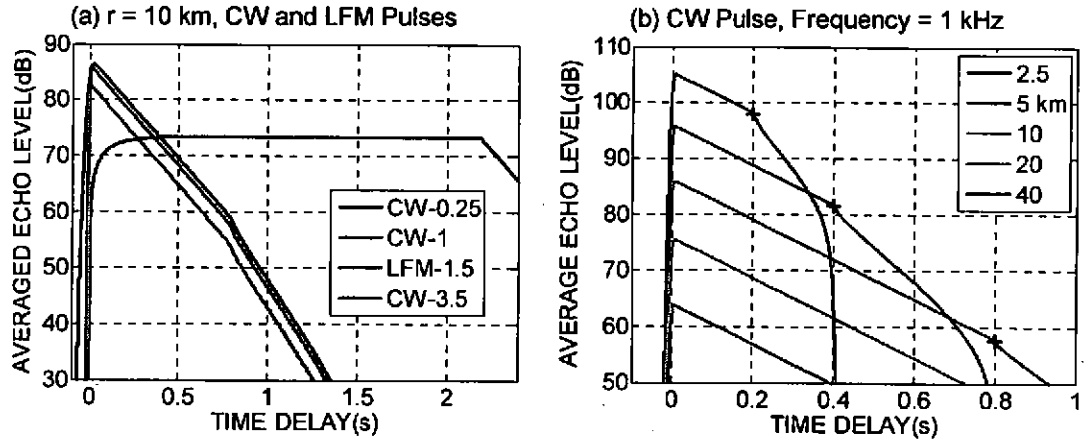

Figure 2. Averaged echo intensities levels (dB // μPa²) at (a) a range of 10 km for the CW and LFM pulses (frequency, kHz) before processing, (b) different ranges for the 1 kHz CW pulse.

2.8 Time Spreading Loss

The total echo energy E_e integrated over all multipath contributions can be written as,

$$E_e(r)=E_0\,S_T\,L_I(r) \tag{19}$$

Where E_0 is the energy flux of the source referenced to 1 m, S_T is the sonar cross section of the target [target strength TS = 10log(S_T)], L_I represents two-way propagation effects integrated over all multipath contributions, [two-way integrated transmission loss 2TL = -10log(L_I)]. For frequencies 1 kHz and above, the ranges of interest are in the multi-mode-stripping region and we use the suitable expressions in Harrison (2003),

$$L_I(r) = \exp(-2\alpha_v r)[2\pi/(\alpha r^3 H)][\mathrm{erf}(W_c)]^2, W_c = [\alpha r/(2H)]^{1/2}\theta_c \quad (20)$$

Where the error function term represent effects of ignoring all energies propagating greater than the critical grazing angle θ_c. We added in-water absorption to Harrison's expressions and the absorption value at the center frequency.

Were all multipaths overlapping, the total intensity of the echo would be

$$I_t(r) \equiv E_e(r)/T_{RE} = I_0 S_T L_I(r) \quad (21)$$

The target can be treated as a point target and the echo intensity envelop is a convolution of the source pulse intensity envelop with the intensity envelope of the channel impulse response. Before and after processing, we approximate the effective time spread of the echo by the summation,

$$\text{Before processing: } \tau_s = T_{RE} + \tau_0 \quad (22)$$

$$\text{After processing: } \tau_s^{MF} = \tau_R + \tau_0 \quad (23)$$

Where T_{RE} and τ_R are given in Table 2. The echo energy is spread over effective time τ_S, τ_S^{MF}, hence the peak echo intensity before and after processing are

$$I_p(r) \equiv E_e(r)/\tau_S \quad (24)$$

$$I_p^{MF}(r) \equiv E_e(r)/\tau_S^{MF} \quad (25)$$

The following ratio can be regarded as the time spreading loss (or gain after pulse compression processing),

$$L_S = I_p(r)/I_t(r) = T_{RE}/\tau_S \quad (26)$$

$$L_S^{MF} = I_p^{MF}(r)/I_t(r) = T_{RE}/\tau_S^{MF} \quad (27)$$

We found that the echo peak levels given by Eqs.(24-25) match closely the peak values from numerical convolution using Eq.(14). The differences are less than 0.1 dB at ranges greater than 5 km and greater at shorter ranges because of the effects of ignoring energies propagating at angles beyond critical.

Figure 3 shows the echo peak intensity level computed for the Gaussian and LFM pulses before [labeled "peak", using Eq.(24)] and after [labeled "MF", using Eq.(25)] matched filtering. The "total" or integrated echo intensity level (the blue curves) given by Eq.(21) were shown for comparison.

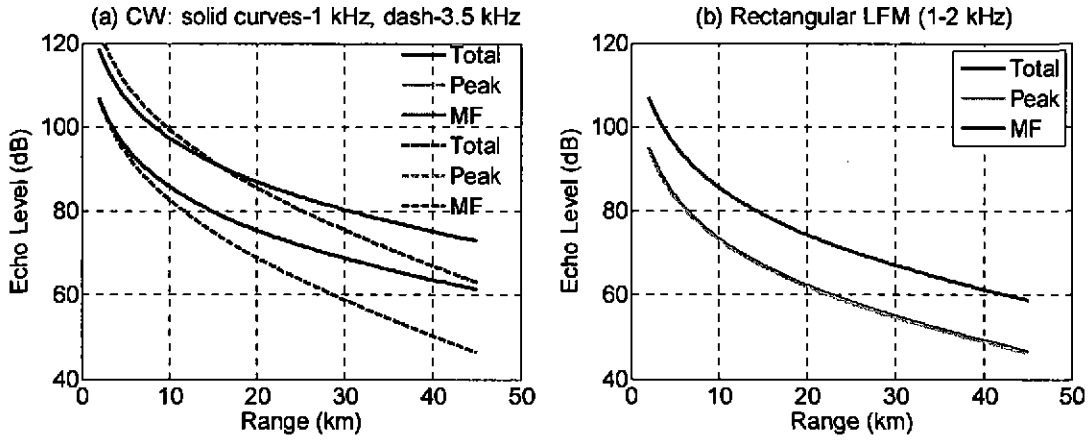

Figure 3. Echo peak intensity level (dB // μPa²) before and after processing for the CW and LFM pulses . The green curves are behind the red curve for the Gaussian pulses in (a) and the blue curve is behind the green curve for the LFM pulse in (b).

For the Gaussian CW pulses, the effective time duration increase by a factor of $2^{1/2}$ after correlation, but the pulse duration both before and after processing are much shorter than the time spread of the channel, hence there is little difference between the peak echo levels before and after processing. The difference between the "total" and the peak levels shows the time spreading loss as defined by Eq.(26). The 3.5 kHz (dashed) curves decay more rapidly with range because of higher absorption.

For the LFM pulse, before processing, the time duration is much greater than the time spread of the channel, all multipaths overlap and the "peak" echo level is essentially the same as the "Total" integrated echo level. After processing. the energy in the 2-sec pulse was compressed to a much shorter effective duration given by τ_S^{MF} in Eq.(23), which is essentially the time spread τ_0 of the channel impulse response because the compressed pulse duration $\tau_R << \tau_0$. There is a corresponding pulse compression gain given by Eq.(27) and shown by the red curve in Fig.3b.

2.9 Reverberation

There are also multipath time spread from each reverberation scattering patch. However, unlike scattering from a finite sized target, the multipaths from continuous extended scatterers (e.g.,the sea floor) overlap and the reverberation power includes multipath arrivals from nearby scattering elements. Hence we ignore time spreading loss for reverberation.

Reverberation intensity before beamformer can be computed using the expression in Harrison (2003, Table III):

$$I_R = (I_0 T_{RE})(\Phi \mu c/(2\alpha^2 r^3)]\exp(-2\alpha_v r)[1-\exp(-W_c^2)]^2 \quad (28)$$

Where, $I_0 T_{RE} = E_0$ is the energy flux of the source at 1 m, μ is the scattering factor of the Lambert's rule, and Φ is the horizontal beamwidth of the source. For the Test Case, $\mu = 10^{-2.7}$, $\Phi = 2\pi$.

Reverberation intensity after beamforming is traditionally modelled by summing the contributions of scatterers ensonified by multipaths within the source and receiver beam pattern. The calculation uses composite beam patterns of source and receiver directivity and there is no need to use a separate receiver array gain. In the test case, the source is omni-directional, the reverberation integral with composite beam patterns de-couple into a reverberation power term from the source as 2D azimuthal isotropic noise at zero grazing angle, divided by the receiver array gain. We computed the reduction in reverberation power by the beamformer in the ambient noise section and those values are used in the following signal to noise ratio (SNR) calculations.

2.10 Signal to Noise Ratio After Processing

For echo detection, Receiver Operating Characteristics relating the required SNR to probabilities of detection and false alarms are often parameterized by the SNR at the *peak* of the matched filter output, using either *instantaneous* signal power [e.g., DiFranco & Rubin (1968), Stewart et al (1959), Westerfield et al (1960)] or mean-square signal power [e.g., Blake(1984)]. The signal is assumed to be deterministic and when the bandwidth of the signal is small compared to the centre frequency, the mean-square signal power over a carrier cycle is half of the *instantaneous* signal power. (Or alternatively, the signal power is half of that of its envelope because adding the quadrature components doubles the signal power.) There is a difference of 3 dB in SNR. A related factor which also causes a 3 dB difference is if the noise power spectral density is defined as one-sided (noise power per unit bandwidth) or two-sided.

Signal detectability, which is determined by the probability distributions of noise and signal plus noise, is unaffected by which definition of SNR is used to parameterize the probability density functions. Care is needed to ensure that the modelled SNR is consistent with that parameterizes the receiver operating characteristics.

In this paper, we define SNR as the mean signal power at the peak of the correlator output over one-sided mean noise power. This definition of SNR can be written in terms of ratios of energy,

$$\mathrm{SNR}_{\mathrm{MF}} = \frac{E_e(\tau_R / \tau_S^{MF}) g_s}{N_0 g_n + I_R \tau_R g_R} \tag{29}$$

Where $W = 1/\tau_R$ is the effective bandwidth defined by Burdic (Sec.8.4, 1991) or the frequency span defined by Woodward (1953) and Westerfield (1960). As discussed earlier, g_s is assumed to be unity in this paper and g_n, g_R represents reductions of the noise and reverberation by the beamformer. The ratio of Eq.(29) is the echo energy contained in a time resolution cell of τ_R among a time spread signal of τ_S^{MF} duration, over noise spectral density $N_0 g_n$ plus reverberation spectral density $I_R g_R / W$, which is also the reverberation energy in a time resolution cell of τ_R.

Eq.(29) may also be written as a ratio of power,

$$\mathrm{SNR}_{\mathrm{MF}} = \frac{I_p^{MF} g_s}{N_0 W g_n + I_R g_R} \tag{30}$$

The interpretation of Eq.(30) is the peak echo power over the summation of noise power in a bandwidth of W, $N_0 W g_n$, and the reverberation power $I_R g_R$. This form of SNR ratio is consistent with the scaling of the matched filter as in Westerfield (1960).

If there is no channel spreading $\tau_0 = 0$ and in reverberation-limited conditions, Eq.(30) may be simplified to

$$\mathrm{SNR}_{\mathrm{MF}} = \frac{I_t g_s}{I_R (\tau_R / T_{RE}) g_R} \tag{31}$$

The denominator of the Eq.(31) has the familiar interpretation of reverberation power due to a pulse of time resolution τ_R.

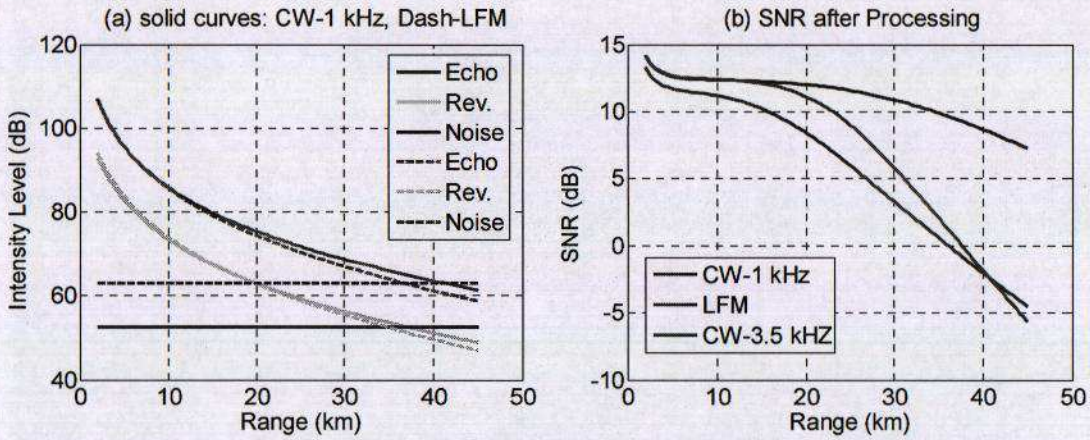

Figure 4. (a) peak echo, reverberation, and noise intensity levels after processing (dB // μPa²) for the Gaussian CW 1 kHz (solid curves) and LFM (dashed curves) pulses. (b) SNR after processing.

Figure 4 shows the peak echo, reverberation, noise power levels after processing and the resultant SNR, computed using Eq.(30), where as discussed earlier in section 2.4, to ease comparison with other modeling results, we assumed $g_s = 1$. We note that the peak echo and reverberation levels of the LFM pulse are similar to those of the Gaussian 1 kHz pulse, but slightly lower due to higher

absorption. However, the noise power of the LFM pulse is greater because of its wider bandwidth, leading to the lower SNR shown in Fig.4(b).

3 LIMITATIONS AND DISCUSSIONS

3.1 Multipath Time Spacing and Pulse Resolution

The time spacing between the multipaths depends on source, receiver and water depths and increases with their grazing angles. At a typical range of 10 km, our calculations based on geometric considerations show that for the LFM pulse, most of the multipaths were well resolved. The exceptions are the direct and surface reflected ray, which has very small time separations due to the closeness of the source and receiver depths. For the 1 kHz and 3.5 kHz Gaussian pulses, near zero grazing angle, the pulses are tightly packed with overlapping and near the effective angle, they are well separated. For the 250 Hz Gaussian pulse, the pulses are mostly overlapping.

Our approach assumed echo energy is continuously distributed from zero to effective angle. When the pulses are overlapping, our predictions ignore the coherent constructive interferences between multipaths and give averaged intensity. When the pulses are well-separated, our predictions under-estimate the peak echo intensity.

3.2 Bottom Phase Shift, Surface Loss, and In-water Absorption

The effects of bottom reflection phase shift can be accounted for by adding an effective depth [Weston (1994)]. The correction is less than a wavelength and for the frequencies concerned, this correction is small.

The loss coefficient in Eq.(11) may be used to extend echo and reverberation expressions previously derived for bottom loss only [e.g., Harrison (2003)] to include effects of surface loss and water absorption.

4 CONCLUDING REMARKS

We predicted the signal to noise ratio for benchmark scenario A2.I using analytical methods, highlighting the importance of echo correlation and time spreading losses. The analytical approach complements predictions using numerical models.

We note that signal to noise ratios are statistical descriptors up to second moments of the probability density functions of signal and noise and thus are incomplete measures of detection performance, which are ultimately determined by the receiver operating statistics.

5 REFERENCES

1. APL-UW (1994), High-Frequency Ocean Environmental Acoustic Models Handbook, Technical Report APL-UW TR 9407, AEAS 9501.
2. Blake, L. V. (1986). Radar Range Performance Analysis. Artech House.
3. Burdic, W.S. (1991), Underwater Acoustic System Analysis (Prentice-Hall,NJ), 2nd Ed.
4. Carey, W. M. (1998), "The determination of signal coherence length based on signal coherence and gain measurements in deep and shallow water," J. Acoust. Soc. Am. 102, 831–837.
5. Cox, H. (1973), 'Line array performance when the signal co-herence is spatially dependent', J. Acoust. Soc. Am. 54, 1743–1746.
6. Desharnais, F. and D.M.F. Chapman (1999), "Vertical coherence of the shallow water ambient noise field, a model", DREA Technical Memorandum 1999-011.
7. Harrison C.H. (2003), "Closed-form expressions for ocean reverberation and signal excess with mode-stripping and Lambert's law," J. Acoust. Soc. Am. 114, 2744-2756.
8. Harrison, C. H., and Nielsen, P. L. (2007). "Multipath pulse shapes in shallow water: Theory and simulation," J. Acoust. Soc. Am. 121, 1362–1373.
9. Jones, A, Duncan, AJ, and Maggi, AL 2007, "Robust prediction of spatial statistics of acoustic field for shallow oceans", Conference Proceedings "Underwater Acoustic Measurements: Technologies & Results", Crete, Greece, June (2007).
10. Prior, M. K., and Harrison, C. H. (2004). "Estimation of seabed reflection loss properties from direct blast pulse shape," J. Acoust. Soc. Am. 116, 1341–1344.
11. Ratilal, P., Lai, Y., and Makris, N.C. (2002), "Validity of the sonar equation and Babinet's principle for scattering in a stratified medium", J. Acoust. Soc. Am. 112, 1797.
12. DiFranco, J.V. and Rubin, W.L. (1968), "Radar Detection", Prentice-Hall.
13. Stewart, J.L., and Westerfield, E.C. (1959), "A theory of active sonar detection", Proc. IRE, 47, pp. 872-881.
14. Stanton, T. K. and Chu, D. (2008), "Calibration of broadband active acoustic systems using a single standard spherical target", J. Acoust. Soc. Am. 124, 128-136.
15. Westerfield, E.; Prager, R.; Stewart, J. (1960); "Processing gains against reverberation (clutter) using matched filters," IRE Transactions on Information Theory, 6, 342-348.
16. Weston, D. E. (1965). "Correlation Loss in Echo Ranging," J. Acoust. Soc. Am. 37, 119-124.
17. Weston, D. E. (1971). "Intensity-range relations in oceanographic acoustics," J. Sound Vib. 18, 271–287.
18. Weston, D.E. (1994). "Wave shifts, beam shifts, and their role in modal and adiabatic propagation," J. Acoust. Soc. Am. 96, 406-416.
19. Wille, P and Thiele, R. (1971), "Transverse Horizontal Coher-ence of Explosive Signals in Shallow Water", J. Acoust. Soc. Am. 50, 348-353.
20. Woodward, P. M. (1964), Probability and Information Theory with Applications to Radar, 2nd edition, Oxford: Pergamon Press.
21. Sun, Z., Gimenez, G., Vray, D., and Denis, F. (1991), "Calculation of the impulse response of a rigid sphere using the physical optic method and modal method jointly," J. Acoust. Soc. Am. 89, 10-18.
22. Zampolli, M. and Ainslie, M. (2010), "Scenarios for benchmarking range-dependent active sonar performance models", this proceedings.
23. Zhang, Z. Y (2009), "Estimating sonar system losses due to signal spatial decorrelation", Conference Proceedings, Australian Acoustical Society, 23-25 November 2009, Adelaide, Australia.
24. Ziomek, L. J (1995), Fundamentals of acoustic field theory and space-time signal processing, CRC Press, Boca Raton.